Official journal of the CIOMP 2047-7538
www.nature.com/lsa

ARTICLE Open Access

# Multifunctional resonant wavefront-shaping meta-optics based on multilayer and multi-perturbation nonlocal metasurfaces

Stephanie C. Malek[1], Adam C. Overvig[1,2], Andrea Alù[2,3] and Nanfang Yu[1]✉

**Abstract**

Photonic devices rarely provide both elaborate spatial control and sharp spectral control over an incoming wavefront. In optical metasurfaces, for example, the localized modes of individual meta-units govern the wavefront shape over a broad bandwidth, while nonlocal lattice modes extended over many unit cells support high quality-factor resonances. Here, we experimentally demonstrate nonlocal dielectric metasurfaces in the near-infrared that offer both spatial and spectral control of light, realizing metalenses focusing light exclusively over a narrowband resonance while leaving off-resonant frequencies unaffected. Our devices attain this functionality by supporting a quasi-bound state in the continuum encoded with a spatially varying geometric phase. We leverage this capability to experimentally realize a versatile platform for multispectral wavefront shaping where a stack of metasurfaces, each supporting multiple independently controlled quasi-bound states in the continuum, molds the optical wavefront distinctively at multiple wavelengths and yet stay transparent over the rest of the spectrum. Such a platform is scalable to the visible for applications in augmented reality and transparent displays.

## Introduction

Metasurfaces—structured planarized optical devices with a thickness thinner than or comparable to the wavelength of light—typically support a "local" response, i.e., they tailor the optical wavefront through the independent response of each meta-unit[1]. In contrast, "nonlocal" metasurfaces are characterized by an optical response dominated by collective modes over many meta-units[2,3]. Local metasurfaces have been widely explored to impart spatially varying phase distributions that shape the impinging optical wavefront to achieve functionalities such as lensing and holography[1,4]. However, these devices have typically limited spectral control: since the optical interactions with the meta-units are confined to deeply subwavelength structures, they are typically broadband, and the wavefront deformation is inevitably extended over a wide frequency range (Fig. 1a left panel). In contrast, nonlocal metasurfaces, such as guided-mode resonance gratings[5,6] and photonic crystal slabs (PCSs)[7,8], can produce sharp spectral features (Fig. 1a middle panel), since they rely on high quality-factor (Q-factor) modes extending transversely over many unit cells. These modes, however, typically cannot at the same time spatially tailor the optical wavefront. Nonlocal metasurfaces hold promise for applications such as sensing[9,10], modulation[11,12], and enhancement of nonlinear optical signals[13,14].

In this work, we design and experimentally realize nonlocal metasurfaces that shape optical wavefronts exclusively at selected wavelengths, leaving the optical wavefront impinging at other wavelengths unchanged (Fig. 1a right panel). Our theoretical work has developed the framework of nonlocal metasurfaces that shape the wavefront only on resonance[15,16]. This is achievable through a scalable rational design scheme previously only

Correspondence: Nanfang Yu (ny2214@columbia.edu)
[1]Department of Applied Physics and Applied Mathematics, Columbia University, New York, NY 10027, USA
[2]Photonics Initiative, Advanced Science Research Center, City University of New York, New York, NY 10031, USA
Full list of author information is available at the end of the article

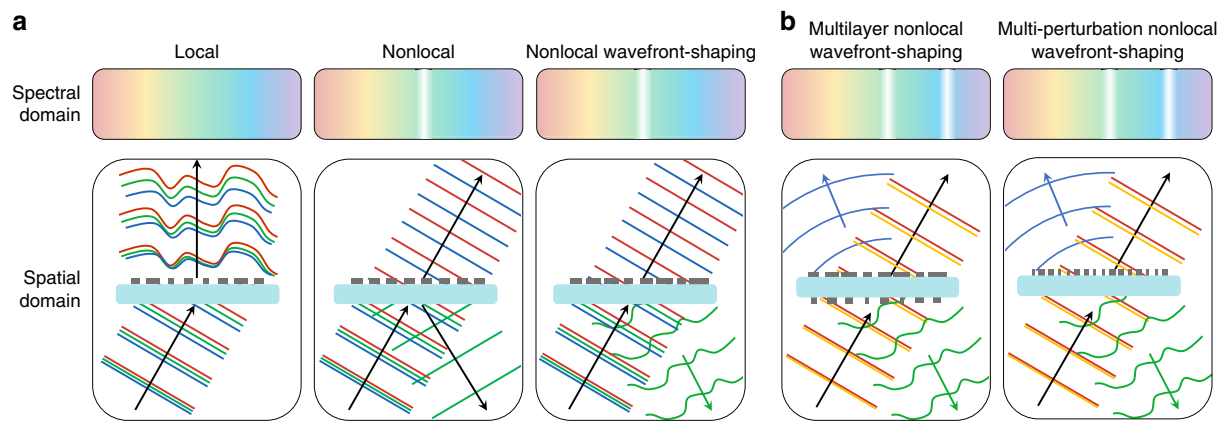


**Fig. 1 Functionality of resonant, wavefront-shaping metasurfaces. a** Schematic illustrating the distinction between three types of metasurfaces. The nonlocal wavefront-shaping metasurface demonstrated in this work provides spatial control exclusively across its sharp spectral features: it molds optical wavefronts only at the resonant frequency, while leaving the optical wavefronts impinging at other frequencies unchanged. **b** Schematic illustrating two approaches to realize multifunctional nonlocal wavefront-shaping meta-optics

available to local metasurfaces, in which the configuration of scatterers across the surface is determined by reference to a precomputed library of meta-units. In this rational design scheme, we can devise single-layer nonlocal metasurfaces that shape wavefronts distinctly at different resonances but leave the wavefront shape unchanged at non-resonant wavelengths (Fig. 1b right panel). We can also stack multiple nonlocal wavefront-shaping metasurfaces together to attain entirely different functionalities at different wavelengths (Fig. 1b left panel). Our theoretical works demonstrated nonlocal metasurfaces with the simple functionalities of single-function cylindrical lensing, multifunctional beam-steering[15,16] and orbital angular momentum manipulation[17,18]. Here, we design and experimentally realize more complex devices including single-function radial lenses and multifunctional lenses based on the two approaches illustrated in Fig. 1b. Our nonlocal radial metalens explicitly demonstrates two-dimensional (2D) spatial control of the wavefront at the resonant frequency, which is not possible based on recent approaches[19] despite the opportunities it presents[20].

## Results

The operating principles of our nonlocal, wavefront-shaping metasurfaces are rooted in the physics of periodic dielectric PCSs that support leaky extended modes. Of particular interest are symmetry-protected bound states in the continuum (BICs), which are modes with infinite radiative Q-factors despite being momentum-matched to free space[8]. Applying a perturbation to break in-plane inversion symmetry of meta-units may create a quasi-BIC (q-BIC) that is leaky and excitable from free space light[21]. Alternatively, a leaky state may be formed using a dimerizing perturbation (i.e., a perturbation that doubles the period along a real-space dimension and halves the first Brillouin zone) that folds a previously guided mode into the radiation continuum (Fig. S1)[22]. In either case, both the scalar and vectorial properties of q-BICs can be readily engineered, and can be controlled with extreme precision through the perturbation. The scalar property of optical lifetime or Q-factor is controlled by the magnitude of the perturbation $\delta$ as $Q \propto \frac{1}{\delta^2}$[21,22]. The vectorial property of polarization is controlled by the type of perturbation, which we have cataloged in our previous theoretical work[15].

In this work, we focus on meta-units (Fig. 2d) from the *p2* plane group—a lattice with two-fold symmetry—because of the special vectorial properties of their q-BICs. Specifically, the in-plane orientation angle $\alpha$ of the dimerizing perturbation dictates that free space light can excite particular q-BIC modes only if it is polarized along the $\phi \sim 2\alpha$ direction (Fig. S2). With circularly polarized light incident at a frequency matching the q-BIC resonance, a device composed of the meta-units becomes a four-port system with ~25% of the incident power sent to each of the ports (i.e., transmitted and reflected light each of converted and preserved handedness of circular polarization). A geometric phase of $\Phi = 2\phi \sim 4\alpha$ is imparted onto transmitted light of converted handedness and reflected light of preserved handedness only at the narrowband q-BIC resonances[15,16]. Therefore, the 2D spatial geometric phase profiles of the radiative component of the q-BIC can be encoded by the 2D spatial distribution of the orientation angle $\alpha$ of the dimerizing perturbation (Supplementary Section 3), while minimally affecting the nonradiative properties of the q-BIC (e.g., near-field mode profile and resonant frequency).

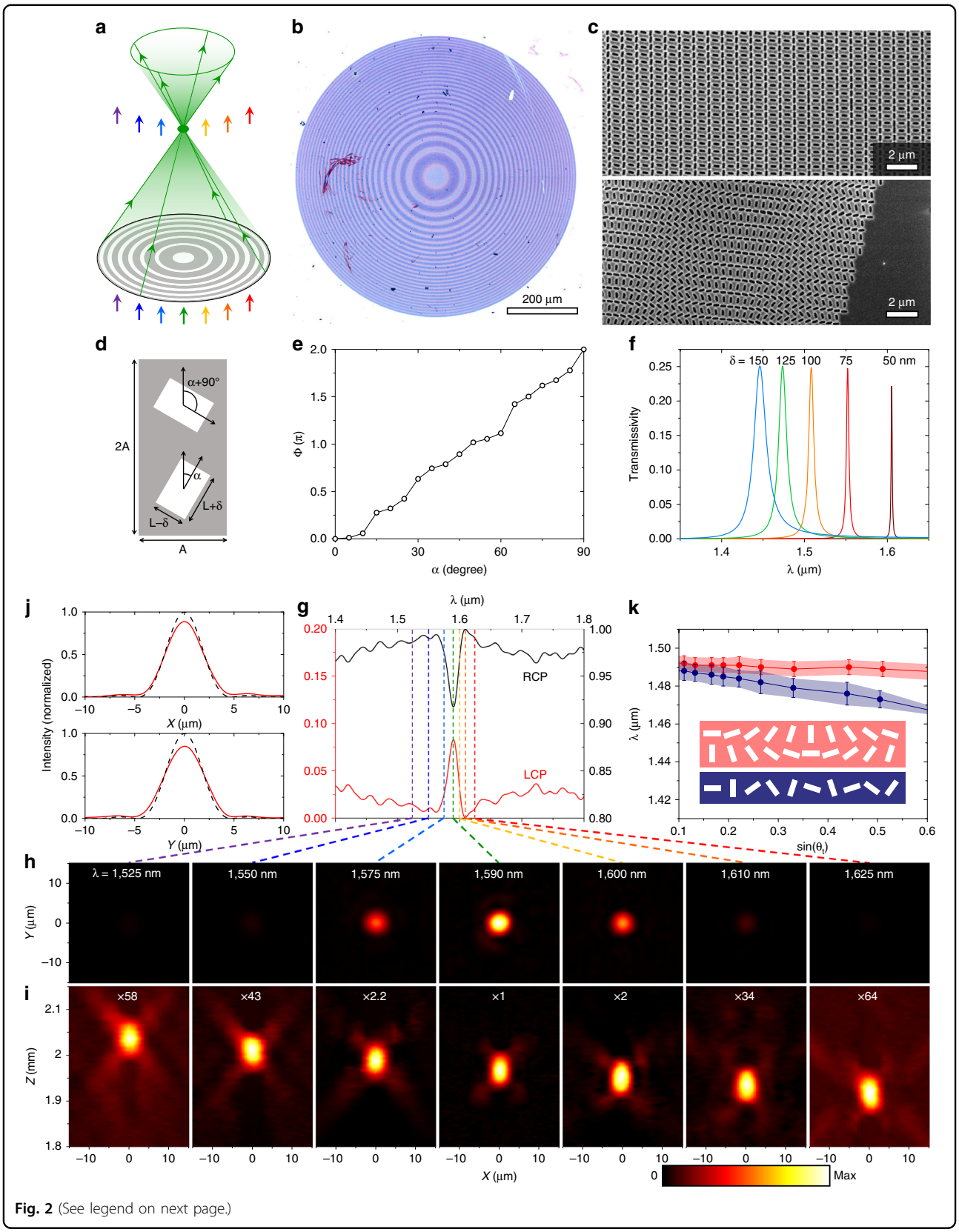


**Fig. 2** (See legend on next page.)

(see figure on previous page)
**Fig. 2 Experimental results of a resonant radial metalens with NA = 0.2. a** Illustration showing the resonant operation of the metalens, with 'green' light being focused, while the other colors are passed without distortion. **b** Photograph of the metalens with a diameter of 800 μm. **c** Scanning electron microscope (SEM) images of the device at its center (top) and edge (bottom). **d** Schematic of a meta-unit of a *p2* plane group, generated by applying a dimerization perturbation of magnitude $\delta$ to a square lattice of square apertures. **e** Simulations showing that the geometric phase $\Phi$ of light of converted handedness of circular polarization is approximately four times of the orientation angle $\alpha$ of the dimerizing perturbation. **f** Spectra of transmitted light with converted handedness of circular polarization of meta-units with $A = 450$ nm, $L = 175$ nm and $\delta = 50$ nm (dark red), $L = 200$ nm and $\delta = 75$ nm (red), $L = 225$ nm and $\delta = 100$ nm (orange), $L = 250$ nm and $\delta = 125$ nm (green), and $L = 275$ nm and $\delta = 150$ nm (blue) defined in a 125 nm thick silicon thin film, showing that Q-factors vary from 3200 (dark red) to 85 (blue). **g** Measured transmission spectra of the metalens for light of converted and unconverted handedness of circular polarization. **h** Measured transverse intensity distributions on the focal plane. **i** Measured longitudinal intensity distributions on a plane through the focal spot. The metalens is located at $Z = 0$. **j** Measured (solid red curves) and theoretical (black dashed curves) linecuts of the focal spot at the center of the resonance, $\lambda = 1590$ nm, along the $x$ and $y$ directions. **k** Simulated resonant wavelength dispersion as a function of refraction angle for phase-gradient nonlocal metasurfaces excited by normally incident light. Dots represent the center of a resonance and shaded regions FWHM of the resonance. Data for the cases in which the phase gradients are orthogonal to the direction of dimerization perturbation are shown in red and those for the cases in which the phase gradients are along the direction of the perturbation are shown in blue. Inset: Schematics illustrating the two alignments between the phase gradient and the dimerization perturbation

In contrast, the recently demonstrated resonant phase-gradient meta-gratings with high Q-factors[19] have been limited to high deflection angles in a single fixed direction relative to the grating. Therefore, the basis of our nonlocal, wavefront-shaping metasurfaces is a library of meta-units (Fig. 2d) where circularly polarized light of converted handedness is transmitted only at narrowband q-BIC resonances and the in-plane orientation angle $\alpha$ controls the geometric phase on resonance (Fig. 2e).

While this geometric phase is fundamentally robust because it stems from symmetry, the meta-unit library must be designed carefully to produce devices that exert accurate spectral and spatial control over the wavefront when fabricated with typical nanofabrication imperfections. The meta-unit library in Fig. 2d aims to achieve a moderate Q-factor for a spectrally isolated q-BIC mode in the near-infrared based on a thin film of amorphous silicon on a glass substrate (Supplementary Section 2). We selected the geometrical parameters of the meta-unit library with the intuition that the thickness of the silicon thin film influences the spectral spacing between fundamental and higher-order q-BICs (Fig. S4), and the perturbation strength controls the Q-factor (Fig. 2f). Figure S3 computationally demonstrates a beam-steering device composed of meta-units from the library.

We experimentally demonstrate (Fig. 2a–c) a nonlocal radial metalens with NA = 0.2 and a diameter of 800 μm using the meta-unit library in Fig. 2d. This metalens has a resonance centered at $\lambda = 1590$ nm with a Q-factor of ~86. The wavelength exclusivity of this feature follows closely with the theoretical expectation: A series of transverse 2D far-field scans shows that focusing is most efficient at the center of the resonance, $\lambda = 1590$ nm, with the focusing efficiency dropping at the two shoulders of the resonance, $\lambda = 1575$ nm and 1600 nm, and that the focal spots become almost undetectable at wavelengths tens of nanometers away from the center of the resonance (Fig. 2h). Longitudinal 2D far-field scans of the device (Fig. 2i) reveal that the focal spots at resonance ($\lambda = 1575$–$1600$ nm) are orders of magnitude brighter than the focal spots off resonance, following a Lorentzian line shape. The device is functionally transparent off resonance in that the background planewave is estimated to be three to four orders of magnitude stronger in power than the focal spots at off-resonance wavelengths. Notably, the focal spot at resonance is diffraction limited: vertical and horizontal linecuts of the focal spot at the center of the resonance (Fig. 2j) reveal Strehl ratios (estimated from the Airy disc and first ring of the intensity pattern) of 0.89 and 0.85 in the $x$ and $y$ directions, respectively. That the lens is diffraction limited suggests that the resonant wavelength is nearly constant across the entire device, otherwise the effective numerical aperture at the resonant wavelength would be smaller than predicted.

Keeping the entire metalens resonant is nontrivial. The unperturbed lattice of the nonlocal metasurface is described by a band structure (Fig. S5); consequently, the resonant wavelengths of the nonlocal modes are dispersive with the deflection angle or phase gradient implemented by the metasurface (Fig. 2k)[15,16]. This represents a key design constraint: the total shift in resonant wavelength due to the phase-gradient variation across a device must be smaller than the full width at half maximum (FWHM) of the resonance. Therefore, given a certain band curvature, there is a tradeoff between the Q-factor and the range of deflection angles supportable across a device, commonly manifested as the numerical aperture (NA) of the metalens[15,16]. The curvature of the most dispersive direction limits the maximum achievable NA. For the simulated meta-unit library of the radial metalens, the estimated maximum NA for a radial metalens is ~0.26 (Fig. 2k). One pathway towards realizing high NA devices is composing a radial lens with

slices of cylindrical lenses using only the least dispersive relative orientation between the phase gradient and the dimerization perturbation (Supplementary Section 5). The ultimate solution is through bandstructure engineering of PCSs[23,24]: a flatter band will allow for the creation of devices with simultaneously higher Q-factors and larger NA.

At the peak of the resonance the device exhibits a maximum conversion efficiency of ~8% of the incident power, as indicated by the circularly polarized transmission spectra in Fig. 2g (unpolarized transmission spectra in Fig. S10). Note that this conversion efficiency is ~32% of the theoretical maximum, which is 25% of the incident power[16,25]. Overcoming the limitation of 25% requires breaking the out-of-plane symmetry. While in principle the presence of a substrate (and absence of a superstrate) meets the requirement, in practice it has little impact on the efficiency. A metasurface partially etched into a high-refractive-index thin film can introduce a larger degree of out-of-plane symmetry breaking[26]. Chiral nonlocal metasurfaces composed of two twisted stacked layers can achieve a theoretical conversion efficiency up to 100% in reflection[27]. In any device architecture, the experimental conversion efficiency may be pushed closer to the theoretical maximum with further refinements to (1) reduce homogeneous broadening of q-BIC resonances caused by fabrication imperfections such as sidewall roughness, and (2) reduce inhomogeneous broadening by limiting long-range disorder across the metasurface (i.e., maintaining precisely the same resonant wavelength across the entire device). The latter in particular may be tackled in our devices by adjusting aperture sizes to compensate for the band curvature during the design process.

Further advances with nonlocal metasurfaces can be achieved by developing multispectral nonlocal meta-optics—either by cascading nonlocal metasurfaces with distinct resonant frequencies, or by adding to a single-layer metasurface a set of orthogonal perturbations, each of which imparts an independent geometric phase profile[16]. We pursue both approaches here, and then show compound meta-optics combining both methods. Beginning with the first approach, we experimentally demonstrate a nonlocal metalens doublet that focuses light at two selected wavelengths and leaves the wavefront shape unchanged at non-resonant wavelengths. This doublet consists of a converging cylindrical lens with NA = 0.1 resonant at a shorter wavelength of $\lambda = 1445$ nm and a diverging radial lens with NA = 0.2 resonant at a longer wavelength of $\lambda = 1580$ nm. They are arranged so that they share the same focal plane located between the two elements (Fig. 3a) but may be rearranged as desired. Both elements are devised from meta-unit libraries of rectangular apertures etched in a 125-nm thick silicon film on glass for convenience, but each element could be based on a distinct material platform or with a different meta-unit motif for more advanced functionalities. The radial lens is the same device as Fig. 2, acting here as a diverging lens because the handedness of circularly polarized incident light has been reversed. Compared to this design, the meta-units for the cylindrical lens, as detailed in Fig. S6, have smaller dimensions to blueshift the resonant wavelength to $\lambda = 1445$ nm. Multiwavelength transverse far-field scans at the focal plane (Fig. 3f) show that at $\lambda = 1445$ nm, one element of the doublet (the cylindrical lens) generates a focal line, while at $\lambda = 1580$ nm, the other element of the doublet (the radial lens) produces a focal spot. Off resonance, there is minimal transmission of handedness-converted light: a plane wave transmits through the doublet with no polarization conversion nor wavefront deformation. This flexible platform featuring narrowband wavefront shaping and broadband transparency can enable many device configurations. For instance, Fig. S15 shows a metasurface doublet where the metalenses do not share a focal plane. Additional functionalities may also be attained by cascading more than two metasurfaces.

In contrast, it is highly nontrivial to cascade conventional local metasurfaces to achieve multifunctionality. To readily cascade metasurfaces and attain different functionalities at different wavelengths, individual metasurfaces must not shape the wavefront at their non-designed wavelength (Fig. S12). In our approach, it is trivial to cascade our nonlocal metasurfaces if their q-BICs do not spectrally overlap. The resulting stack performs the collective functions of all the individual metasurfaces and does not alter the wavefront shape at non-resonant wavelengths. Therefore, the precise lateral and longitudinal alignment of the cascaded metasurfaces relative to each other does not affect the operation of the individual metasurfaces, only the overall functionality of the metasurface stack (e.g., whether the metalenses share a focal plane and whether the focal spots coincide laterally). However, local metasurfaces are usually spectrally broadband, so simply stacking them can result in distorted wavefronts and degraded functionalities (Figs. S13, S14). The stack—rather than individual metasurfaces—must be designed as one entity to perform the desired set of functions (Table S2). Such systems often prove computationally intensive to devise[28–30], require precise lateral alignment of the constituent metasurfaces[29,31], and do not support closely spaced operating wavelengths[31,32].

We also experimentally demonstrate a two-function metasurface based on orthogonal perturbations where each perturbation independently controls one targeted q-BIC. The designed meta-units (Fig. 3k) are formed by two sets of rectangular apertures in a silicon thin film, and each set of apertures controls the phase of one q-BIC but not that of the other. In isolation, each set of apertures

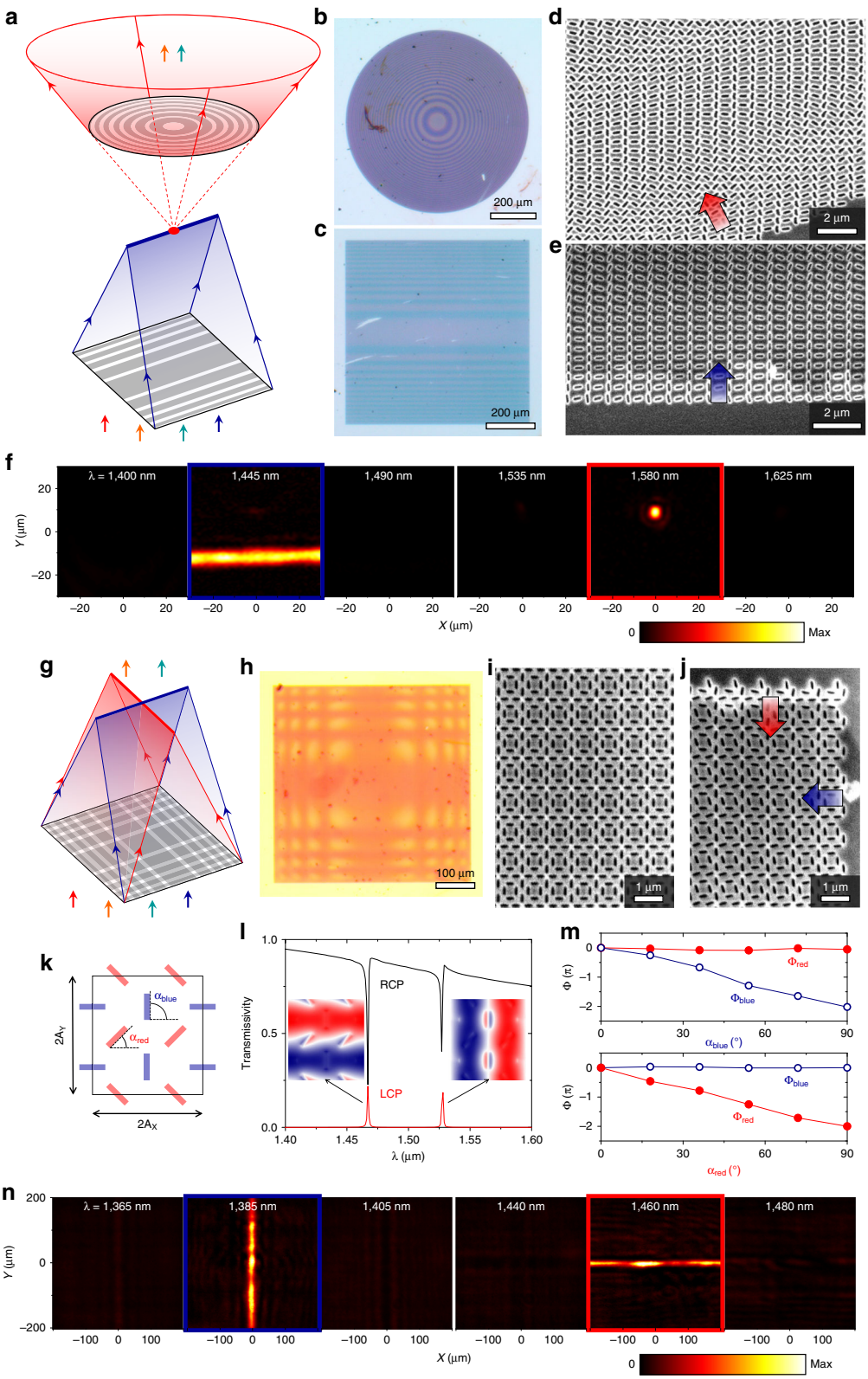


**Fig. 3** (See legend on next page.)

(see figure on previous page)

**Fig. 3 Experimental results of multifunctional meta-optics devised by a multilayer approach (a–f) and a multi-perturbation approach (g–n).** **a** Schematic illustrating the multilayer approach with a cylindrical lens with NA = 0.1 made from the meta-unit library in Fig. S6 as the converging element and the radial lens from Fig. 2 as the diverging element. Photographs of the diverging (**b**) and converging (**c**) elements of the doublet. SEM images of the diverging (**d**) and converging (**e**) elements. Arrows indicate phase gradient direction. **f** Measured transverse intensity distributions of transmitted light of converted handedness of the doublet. **g** Schematic illustrating the multi-perturbation approach for a dual-function cylindrical lens. **h** Optical image of the device. SEM images of the device at the center (**i**) and corner (**j**) of the device. **k** Schematic of a meta-unit of the dual-function cylindrical lens. Shown are two sets of apertures (colored red and blue) defined in a silicon thin film $A_{x\ y}$. **l** Simulated transmission spectra of light with converted (red) and preserved (black) handedness. Insets: Out-of-plane component of electric field for the two modes. **m** Geometric phases of both modes as a function of in-plane rotation angle of the blue (top) and red (bottom) perturbations, respectively. **n** Measured transverse intensity distributions of handedness converted light on the focal plane of the dual-function cylindrical lens. Device dimensions are detailed in Table S1

belong to the *p2* plane group, but together the composite meta-units in this device have only translational symmetry and therefore belong to the *p1* plane group[16]. This follows the principle of successive orthogonal perturbations[16], which is fundamentally distinct from that of spatial multiplexing commonly employed in local[33,34] and nonlocal metasurfaces[35,36] for multifunctionality. Simply multiplexing *p2* meta-units with different operating wavelengths does not achieve the desired multifunctionality (Supplementary Section 9). We note that this meta-unit library (Fig. 3k–m) is designed to have lower Q-factors than the multi-perturbation device in our previous theoretical work[16] in order to implement nonconstant phase gradients and to improve the device robustness against fabrication imperfections. Specifically, the Q-factor varies inversely with the magnitude of the perturbation[22], but simply increasing the latter (e.g., more highly anisotropic apertures) is not always a sufficient or experimentally practical method to achieve a target Q-factor. So in contrast to the purely symmetry driven designs in our initial theoretical proof-of principle demonstration[16], here the motif and height of the meta-units are judiciously chosen.

We devise a metasurface implementing two orthogonal cylindrical lenses (Fig. 3g), both with NA ~ 0.05, where the phase profile for each lens is controlled by only one set of perturbations. An optical microscope image of the fabricated device (Fig. 3h) shows the horizontal and vertical zones of the two lenses overlapping within the single metasurface as a result of the two independently tiled sets of apertures (SEM images: Fig. 3i, j). Imaging handedness-converted light from this device at the shared focal plane reveals a vertical focal line at $\lambda = 1385$ nm, a horizontal focal line at $\lambda = 1460$ nm, and mostly flat wavefronts at nonresonant wavelengths (Fig. 3n). We have therefore demonstrated that both approaches to multifunctional nonlocal meta-optics—cascaded metasurfaces and multiple independent perturbations—are achievable experimentally, with cascading leaving open the possibility of reconfiguring the constituent metasurface elements and multiple perturbations allowing for a thin single-layer, multifunctional device. In principal, up to four distinct functions (e.g., phase profiles) from four distinct q-BICs may be realized on a single metasurface[16], at the cost of denser patterning and increased cross-talk.

These two approaches to multispectral nonlocal meta-optics can be combined to experimentally realize highly multifunctional meta-optics. We begin by assembling a three-function doublet (Fig. 4a) by stacking a dual-function cylindrical lens as a converging element (Fig. 4c, f, g) and a single-function quasi-radial lens as a diverging element (Fig. 4b, d, e) such that the two metasurfaces share a focal plane. The measured transverse intensity distributions on the shared focal plane reveal a horizontal focal line at $\lambda = 1424$ nm and a vertical focal line at $\lambda = 1492$ nm from the dual-function cylindrical lens, a focal spot from the quasi-radial lens at $\lambda = 1626$ nm, and minimal handedness-converted light at other wavelengths (Fig. 4h). The Q-factors for these three lensing functions range from ~60 to ~90 (Fig. 4i).

Further functionality can be realized by cascading more than one multifunctional metasurface, such as a four-function doublet (Fig. 5a) consisting of two dual-function cylindrical lenses (Fig. 5b–e) that share the same focal plane. The measured transverse intensity distributions on the shared focal plane show four distinct focal lines—at $\lambda = 1414$ nm and 1530 nm from the converging element and $\lambda = 1388$ nm and 1460 nm from the diverging element (Fig. 5f). The Q-factors for these four lensing functions range from ~100 to ~300 (Fig. 5g). Our demonstration of highly multifunctional meta-optics features more distinct functionalities per wavelength range and per number of metasurface layers than has been previously reported for cascaded local metasurfaces (Table S2). The degree of multifunctionality can be boosted by stacking many nonlocal metasurfaces each with up to four independent perturbations[16].

The experimental demonstration of these multifunctional devices is challenging compared to local metasurfaces because a near-constant resonant wavelength must be maintained across the entire device. In addition to the aforementioned angular dispersion, the

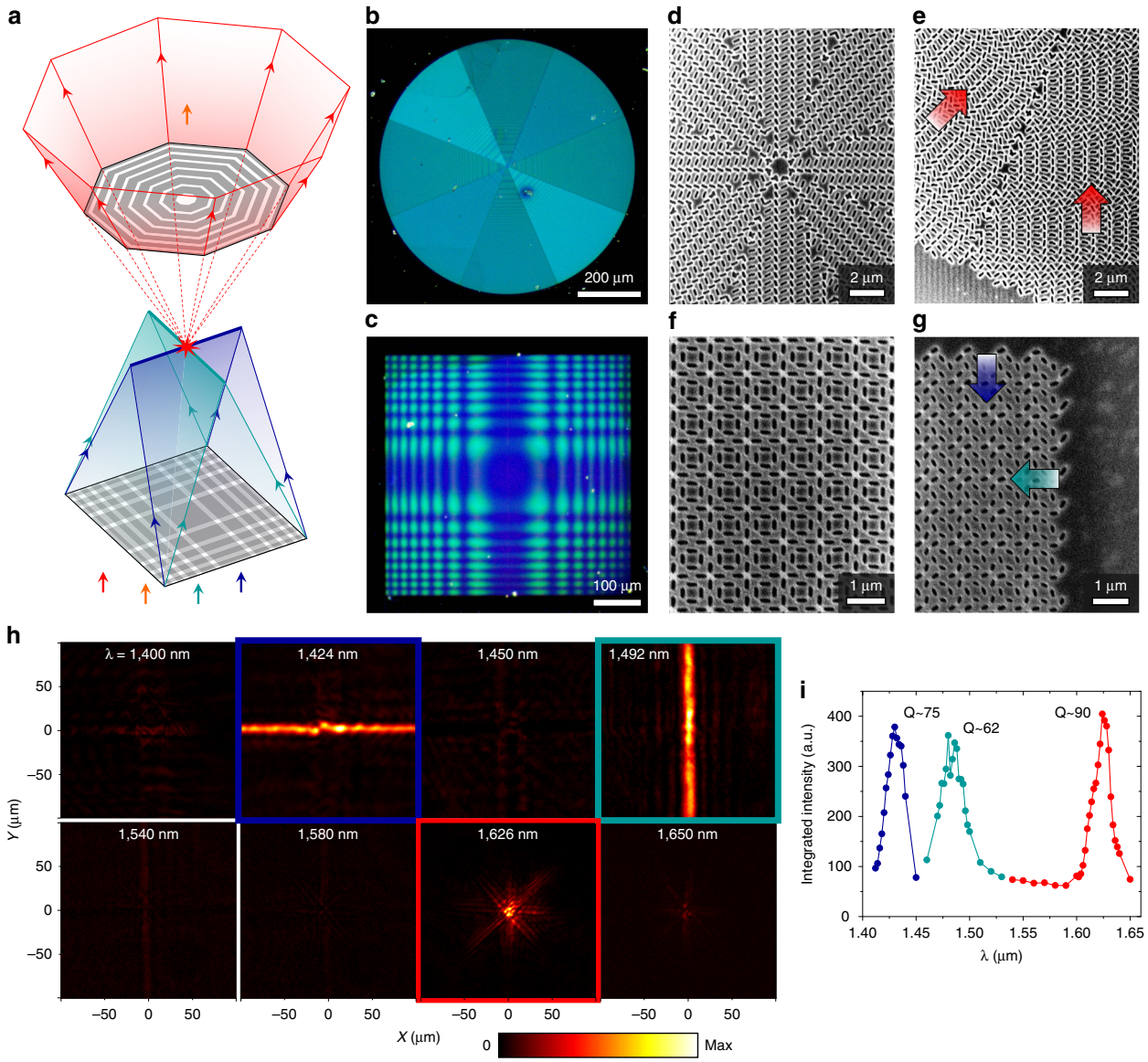


**Fig. 4 Experimental results of a three-function doublet. a** Schematic illustrating the operation of the three-function doublet with a single-function quasi-radial lens with NA = 0.4 as a diverging element and a dual-function metalens (two orthogonal cylindrical lenses, both with NA ~ 0.1) as a converging element. Dark field optical microscope images of the diverging (**b**) and converging (**c**) devices. SEM images of the diverging device at its center (**d**) and edge (**e**). SEM images of the converging device at its center (**f**) and edge (**g**). Arrows indicate phase gradient direction. **h** Measured transverse intensity distributions of handedness-converted light of the doublet at the shared focal plane. **i** Estimated Q-factors for the three lensing functions by integrating the optical intensity over the focal features (focal lines or focal spot) as a function of wavelength (Supplementary Section 10). Device dimensions are detailed in Table S1

resonant frequency could also be affected by the quality of device fabrication. For example, the spatial profiles of the modes in the diverging element in Fig. 5 are such that in-plane components of the electric field are dominant and concentrated within the apertures (Fig. S18). As a result, the resonant wavelengths can vary due to small systematic variations in aperture size across the footprint of the device caused by systematic variations in thin-film deposition, lithographic exposure, or etching conditions. In fact, in devices with large fabrication errors, the q-BICs cannot be excited across their footprint by a monochromatic excitation (e.g., devices regionally resonate with incident light based on the frequency) (Fig. S19).

Finally, we demonstrate in simulations the utility of our multifunctional nonlocal metasurfaces in augmented reality (AR) glasses operating in the visible. Due to their small form-factor and expanded functionality compared to conventional optical components, metasurfaces have

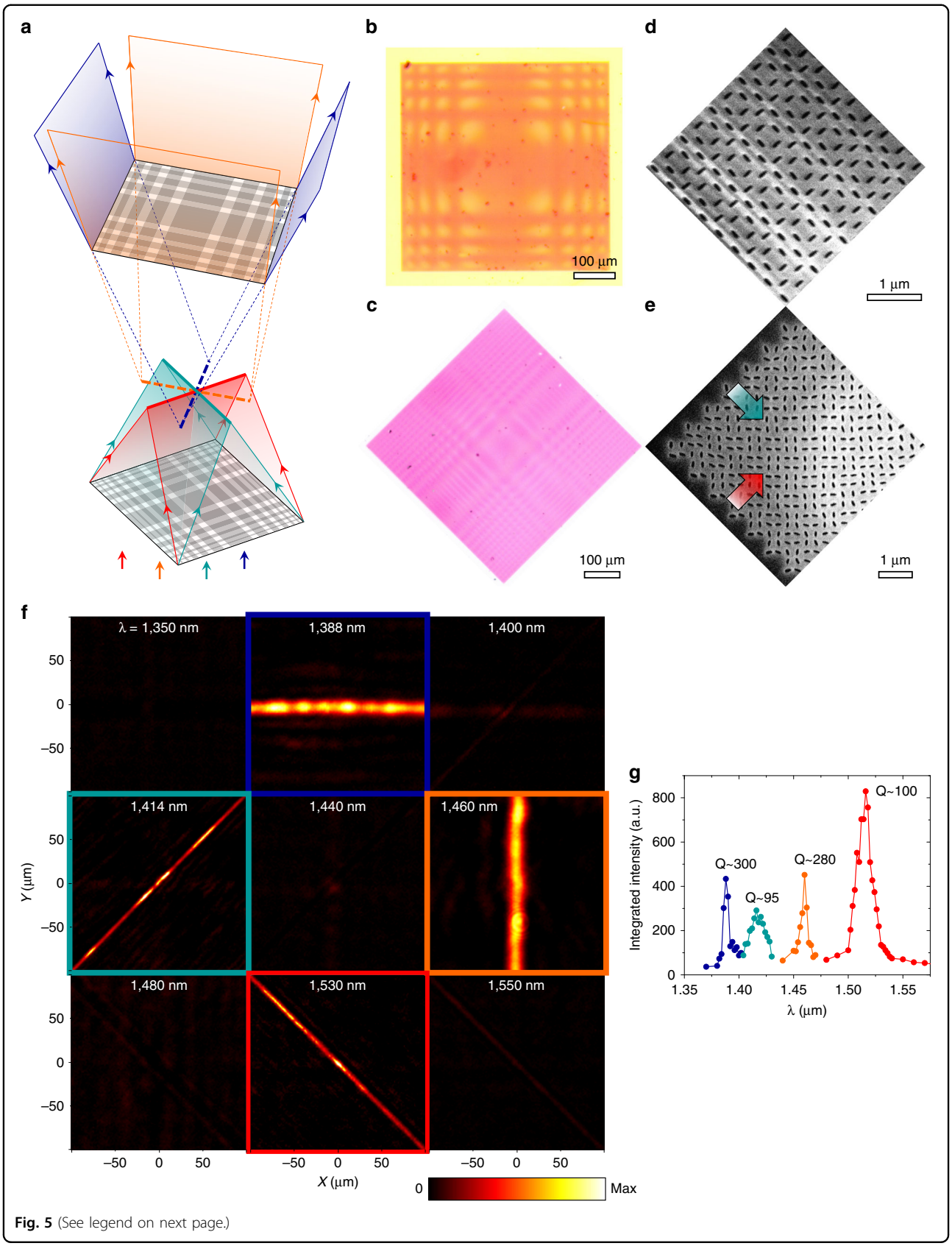


**Fig. 5** (See legend on next page.)

(see figure on previous page)

**Fig. 5 Experimental results of a four-function doublet. a** Schematic of the doublet composed of a dual-function cylindrical lens with NA ~ 0.14 as the converging element and the multi-perturbation device in Fig. 3 with NA ~ 0.05 as the diverging element. Bright field optical microscope images of the diverging (**b**) and converging (**c**) elements. SEM images of the diverging element at its center (**d**) and converging element at its corner (**e**). Arrows indicate the direction of the phase gradient. **f** Measured transverse intensity distributions for the four-function doublet at the shared focal plane. **g** Estimated Q-factors for the four lensing functions by integrating the optical intensity over the focal features (focal lines) as a function of wavelength (Supplementary Section 10). Device dimensions are detailed in Table S1

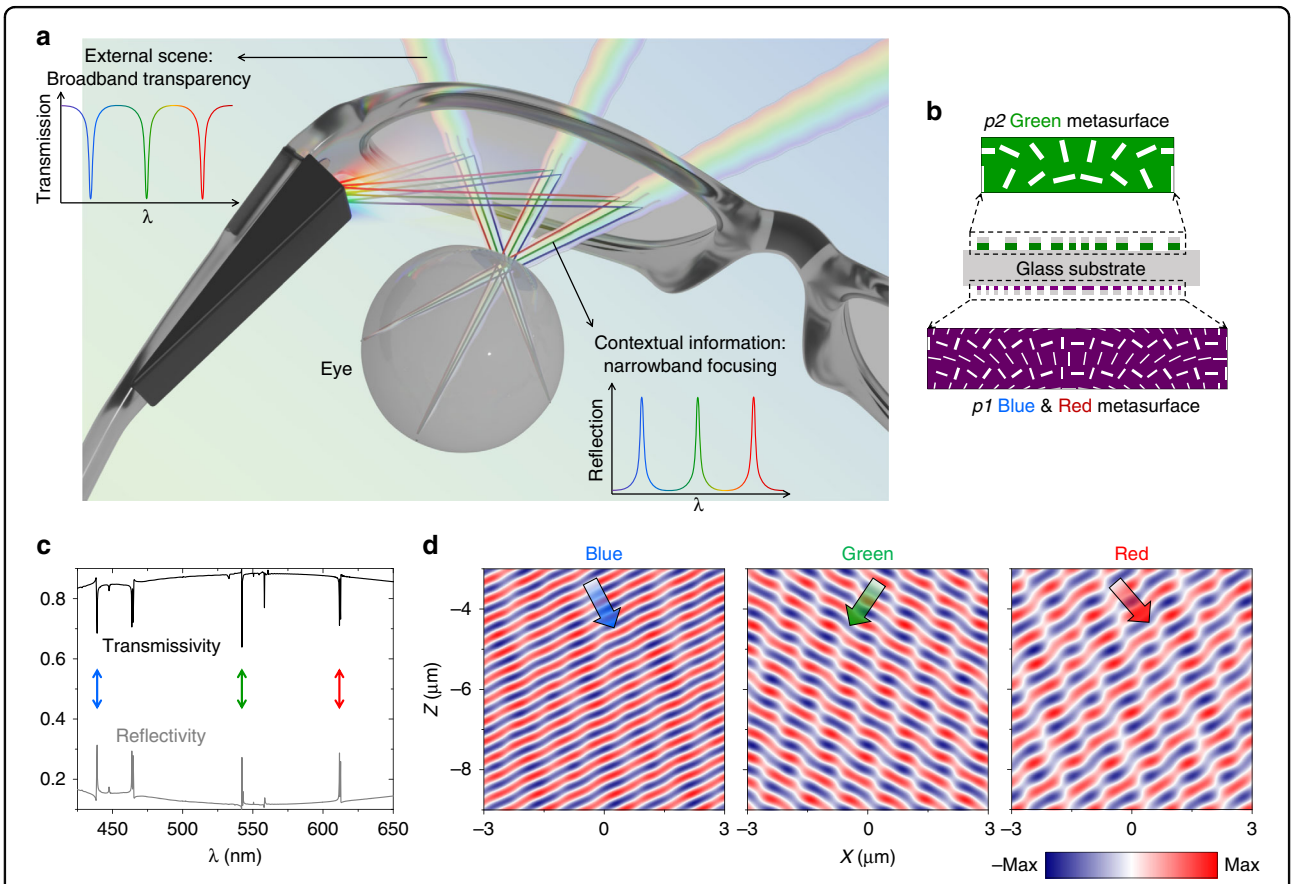


**Fig. 6 Conceptual demonstration of AR enabled by multifunctional nonlocal metasurfaces. a** Illustration showing the operation of an AR headset with multifunctional nonlocal metasurfaces as optical see-through lenses. **b** Schematic of a super-period of a nonlocal meta-optics system implementing three distinct phase gradients at three chosen visible wavelengths, respectively. See Table S1 for detailed design parameters. **c** Simulated transmission and reflection spectra of the meta-optics system. Arrows indicate three TE q-BICs for wavefront shaping at the three colors. Additional spectral features correspond to TM modes associated with the chosen TE modes or result from subtle symmetry-breaking introduced by meshing during full-wave simulations. **d** Simulated reflected wavefronts shaped by independent q-BICs at $\lambda_B = 439$ nm, $\lambda_G = 542$ nm, and $\lambda_R = 612$ nm. Arrows indicate light propagation directions at the three colors

attracted growing interest for applications in AR headsets[37–40]. Thus far, most reported metasurfaces for AR require extra optical components, such as polarizers or beam splitters, that inevitably attenuate real-world light and add size and mass to the headset (Table S3). Figure 6a schematically shows our nonlocal metasurface acting as an optical see-through lens that reflects contextual information to the viewer's eye at selected narrowband wavelengths but permits an unobstructed broadband view of the real world. This paradigm allows for a wide field of view of contextual information with the nonlocal metasurface covering the entire eyeglass, and does not require extra polarizers or beam-splitters that attenuate real-world light.

As a proof of concept, we design and numerically demonstrate a nonlocal meta-optics system on a single glass substrate that independently controls the anomalous reflection of three colors of contextual information while remaining transparent to impinging light from the real world (Fig. 6a). This design entails a doublet with a

single-function metasurface based on *p2* meta-units operating at the green wavelength and a dual-function metasurface based on *p1* meta-units operating at the red and blue wavelengths (Fig. 6b). Both metasurfaces are composed of rectangular apertures etched into a thin film of $TiO_2$ covered with an antireflection layer of $SiO_2$ and are compatible with previously demonstrated fabrication methods[41,42]. Figure 6c highlights the broadband high-transmission of real-world light and the narrowband reflection at the three chosen wavelengths in the visible for the doublet, calculated by finite-difference time-domain simulations and an incoherent transfer matrix method[43]. The simulated wavefronts of reflected light on resonance are independently and deliberately steered by the doublet (Fig. 6d).

This design demonstrates a pathway towards future applications of our nonlocal metasurfaces but leaves several areas for future improvements. First, chiral nonlocal metasurfaces[27] can be used to realize near-unity reflection of contextual information to the eye without transmission of stray contextual information through the lens. Second, further optimization of the thickness of the metasurface (Fig. S4) or the meta-unit motif may control the spectral spacing between fundamental and higher-order modes or between TE and TM modes of the same order to effectively minimize unwanted modes in the visible spectrum. Alternatively, wavelength-dependent material absorption can be used to suppress undesired resonant modes[39]. These unwanted modes inevitably shape the wavefront of spectrally narrow bands of light and may introduce some distortion to a very small portion of the visible spectrum. Finally, we envision that band-structure engineering can achieve flatter bands that will enable high NA lenses for practical AR solutions.

## Discussion

We have experimentally demonstrated nonlocal wavefront-shaping metasurfaces and meta-optics systems including a nonlocal radial metalens, a dual-function cylindrical metalens, and metalens doublets with up to four distinct functionalities. This platform of nonlocal metasurfaces readily allows for independent control of resonant wavelengths (via meta-unit geometry), Q-factors (via perturbation strength), resonant frequency dispersion (via bandstructure engineering), and wavefront (via spatial distribution of geometric phase) at a plurality of wavelengths (via cascading metasurfaces and/or adding independent perturbations to individual metasurfaces). These devices may expand the capabilities of multifunctional meta-optics to include active or nonlinear wavefront shaping by leveraging the enhanced light-matter interactions of the high Q-factor, wavefront-shaping resonances[44]. In addition, incorporating local metasurface design considerations may allow us to realize multifunctional wavefront generation from structured thin films driven by incoherent emitters[18]. The concept of wavefront-shaping with q-BICs is also applicable to waveguide-integrated metasurfaces[45] and is the subject of future work. Scaled to visible wavelengths, our resonant metasurfaces may prove useful for AR and transparent display applications as compact multi-color see-through optics.

## Materials and methods

### Device fabrication

Approximately 100, 125, or 200 nm of amorphous silicon (a-Si) is deposited on a fused silica wafer by plasma enhanced chemical vapor deposition (Oxford Instruments NPG90 PECVD). The wafer is spin-coated with poly(methyl methacrylate) (PMMA A4 950) for 45 s at 2000 RPM and then baked at 180 °C for 2 min. Then an anti-charging layer, DisCharge H2O (DisChem, Inc.), is spun at 2000 RPM for 45 s. Devices are patterned with electron beam lithography (Elionix ELS-G100) at a current of 1 nA for the radial lenses and 2 nA for the cylindrical lenses after appropriate proximity effect correction is applied (BEAMER). After exposure, the anti-charging layer is removed by rinsing in DI water, and the devices are developed in a chilled 3:1 isopropyl alcohol:deionized water solution for 2 min followed by 30 s of rinsing in deionized water. The devices are etched in a fluorine-based inductively coupled plasma etcher (Oxford Instruments PlasmaPro 100). The PMMA etch mask is stripped by soaking the wafer in N-Methyl-2-pyrrolidone at 80 °C for several hours.

### Transmission measurements

Transmission spectra are measured with a Fourier transform infrared spectrometer (Bruker Vertex 70 v) and a mid-infrared microscope (Bruker Hyperion 2000) with two circular polarizers (Thorlabs) in the beam path—the first one circularly polarizes the incident light and the second selects the handedness of the light transmitted through the device. Raw data is normalized with the following scheme to obtain polarization converted ($T_c$) and unconverted ($T_u$) transmission spectra.

$$A = \textit{converted polarization on device} - \textit{converted polarization on unpatterned wafer}$$

$$B = \textit{unconverted polarization on device} + A$$

$$T_c = \frac{A}{B}$$

$$T_u = \frac{\textit{unconverted polarization on device}}{B}$$

The above procedure will yield more accurate spectra as the infrared objectives used in our spectroscopic setup

introduce some degree of background polarization conversion. Normalized transmission spectra are filtered with a fast Fourier transform filter to remove fine fringes due to Fabry–Pérot interference of light in the substrate.

## Far field intensity scans

The focusing performance of the metalenses is measured according to the framework described in our previous work[46]. Near-infrared light is coupled from a super continuum source (NKT Photonics SuperK Extreme) through a monochromator (Horiba iHR550) to a fiber collimator and then circularly polarized by properly orienting a linear polarizer and a quarter-wave plate. Light transmitted through the metasurface is collected by a 10× objective and one of its circularly polarized components is selected by another quarter-wave plate and linear polarizer before it is imaged by a near-infrared camera (NIRvana InGaAs camera, Princeton Instruments). The objective, analyzing polarizer, quarter-wave plate, and camera are all mounted on a motorized linear translation stage. With the latter, two-dimensional transmitted intensity patterns are imaged over a 1–2 mm longitudinal range around the focal plane of the metalenses in steps of 1–5 μm at a number of selected wavelengths. A three-dimensional intensity pattern can be created by stacking a series of such two-dimensional intensity patterns.

#### Acknowledgements
This work was supported by the National Science Foundation (grant no. QII-TAQS-1936359 and no. ECCS-2004685) and the Air Force Office of Scientific Research (grant no. FA9550-14-1-0389 and no. FA9550-16-1-0322). S.C.M. acknowledges support from the NSF Graduate Research Fellowship Program (grant no. DGE-1644869). A.C.O. acknowledges support from the NSF IGERT program (grant no. DGE-1069240). Device fabrication was carried out at the Columbia Nano Initiative cleanroom, and at the Advanced Science Research Center NanoFabrication Facility at the Graduate Center of the City University of New York.

#### Author details
[1]Department of Applied Physics and Applied Mathematics, Columbia University, New York, NY 10027, USA. [2]Photonics Initiative, Advanced Science Research Center, City University of New York, New York, NY 10031, USA. [3]Physics Program, Graduate Center, City University of New York, New York, NY 10016, USA

#### Author contributions
S.C.M. and N.Y. conceived the experiments. S.C.M. and A.C.O. conducted analytical calculations and full-wave simulations to design the devices. S.C.M. fabricated the devices, constructed the experimental setup, and characterized device performance. S.C.M., A.C.O., and N.Y. analyzed the data. A.A. and N.Y. supervised the project. All authors prepared and edited the manuscript.

#### Conflict of interest
The authors declare no competing interests.

**Supplementary information** The online version contains supplementary material available at https://doi.org/10.1038/s41377-022-00905-6.

Received: 13 February 2022 Revised: 11 June 2022 Accepted: 20 June 2022
Published online: 03 August 2022

#### References
1. Yu, N. & Capasso, F. Flat optics with designer metasurfaces. *Nat. Mater.* **13**, 139–150 (2014).
2. Kwon, H. et al. Nonlocal metasurfaces for optical signal processing. *Phys. Rev. Lett.* **121**, 173004 (2018).
3. Monticone, F., Valagiannopoulos, C. A. & Alù, A. Parity-time symmetric nonlocal metasurfaces: all-angle negative refraction and volumetric imaging. *Phys. Rev. X* **6**, 041018 (2016).
4. Genevet, P. et al. Recent advances in planar optics: from plasmonic to dielectric metasurfaces. *Optica* **4**, 139–152 (2017).
5. Chang-Hasnain, C. J. & Yang, W. High-contrast gratings for integrated optoelectronics. *Adv. Opt. Photonics* **4**, 379–440 (2012).
6. Wang, S. S. & Magnusson, R. Theory and applications of guided-mode resonance filters. *Appl. Opt.* **32**, 2606–2613 (1993).
7. Johnson, S. G. et al. Guided modes in photonic crystal slabs. *Phys. Rev. B* **60**, 5751–5758 (1999).
8. Sakoda, K. Symmetry, degeneracy, and uncoupled modes in two-dimensional photonic lattices. *Phys. Rev. B* **52**, 7982–7986 (1995).
9. Tittl, A. et al. Imaging-based molecular barcoding with pixelated dielectric metasurfaces. *Science* **360**, 1105–1109 (2018).
10. Leitis, A. et al. Angle-multiplexed all-dielectric metasurfaces for broadband molecular fingerprint retrieval. *Sci. Adv.* **5**, eaaw2871 (2019).
11. Karl, N. et al. All-optical tuning of symmetry protected quasi bound states in the continuum. *Appl. Phys. Lett.* **115**, 141103 (2019).
12. Forouzmand, A. & Mosallaei, H. A tunable semiconductor-based transmissive metasurface: dynamic phase control with high transmission level. *Laser Photonics Rev.* **14**, 1900353 (2020).
13. Koshelev, K. et al. Subwavelength dielectric resonators for nonlinear nanophotonics. *Science* **367**, 288–292 (2020).
14. Koshelev, K. et al. Nonlinear metasurfaces governed by bound states in the continuum. *ACS Photonics* **6**, 1639–1644 (2019).
15. Overvig, A. C. et al. Selection rules for quasibound states in the continuum. *Phys. Rev. B* **102**, 035434 (2020).
16. Overvig, A. C., Malek, S. C. & Yu, N. Multifunctional nonlocal metasurfaces. *Phys. Rev. Lett.* **125**, 017402 (2020).
17. Overvig, A. & Alù, A. Wavefront-selective Fano resonant metasurfaces. *Adv. Photonics* **3**, 026002 (2021).
18. Overvig, A. C., Mann, S. A. & Alù, A. Thermal metasurfaces: complete emission control by combining local and nonlocal light-matter interactions. *Phys. Rev. X* **11**, 021050 (2021).
19. Lawrence, M. et al. High quality factor phase gradient metasurfaces. *Nat. Nanotechnol.* **15**, 956–961 (2020).
20. Barton, D. et al. High-*Q* nanophotonics: sculpting wavefronts with slow light. *Nanophotonics* **10**, 83–88 (2020).
21. Koshelev, K. et al. Asymmetric metasurfaces with high-*Q* resonances governed by bound states in the continuum. *Phys. Rev. Lett.* **121**, 193903 (2018).
22. Overvig, A. C., Shrestha, S. & Yu, N. Dimerized high contrast gratings. *Nanophotonics* **7**, 1157–1168 (2018).
23. Zong, Y. et al. Observation of localized flat-band states in Kagome photonic lattices. *Opt. Express* **24**, 8877–8885 (2016).
24. Nguyen, H. S. et al. Symmetry breaking in photonic crystals: on-demand dispersion from flatband to Dirac cones. *Phys. Rev. Lett.* **120**, 066102 (2018).
25. Monticone, F., Estakhri, N. M. & Alù, A. Full control of nanoscale optical transmission with a composite metascreen. *Phys. Rev. Lett.* **110**, 203903 (2013).
26. Zhu, A. Y. et al. Giant intrinsic chiro-optical activity in planar dielectric nanostructures. *Light Sci. Appl.* **7**, 17158 (2018).
27. Overvig, A., Yu, N. & Alù, A. Chiral quasi-bound states in the continuum. *Phys. Rev. Lett.* **126**, 073001 (2021).
28. McClung, A., Mansouree, M. & Arbabi, A. At-will chromatic dispersion by prescribing light trajectories with cascaded metasurfaces. *Light Sci. Appl.* **9**, 93 (2020).
29. Georgi, P. et al. Optical secret sharing with cascaded metasurface holography. *Sci. Adv.* **7**, eabf9718 (2021).
30. Zhu, D. et al. Building multifunctional metasystems *via* algorithmic construction. *ACS Nano* **15**, 2318–2326 (2021).
31. Zhou, Y. et al. Multilayer noninteracting dielectric metasurfaces for multiwavelength metaoptics. *Nano Lett.* **18**, 7529–7537 (2018).
32. Avayu, O. et al. Composite functional metasurfaces for multispectral achromatic optics. *Nat. Commun.* **8**, 14992 (2017).
33. Huang, Y. W. et al. Aluminum plasmonic multicolor meta-hologram. *Nano Lett.* **15**, 3122–3127 (2015).

34. Lin, D. et al. Photonic multitasking interleaved Si nanoantenna phased array. *Nano Lett.* **16**, 7671–7676 (2016).
35. Klopfer, E. et al. Dynamic focusing with high-quality-factor metalenses. *Nano Lett.* **20**, 5127–5132 (2020).
36. Spägele, C. et al. Multifunctional wide-angle optics and lasing based on supercell metasurfaces. *Nat. Commun.* **12**, 3787 (2021).
37. Nikolov, D. K. et al. Metaform optics: bridging nanophotonics and freeform optics. *Sci. Adv.* **7**, eabe5112 (2021).
38. Li, Z. et al. Meta-optics achieves RGB-achromatic focusing for virtual reality. *Sci. Adv.* **7**, eabe4458 (2021).
39. Song, J. H. et al. Non-local metasurfaces for spectrally decoupled wavefront manipulation and eye tracking. *Nat. Nanotechnol.* **16**, 1224–1230 (2021).
40. Brongersma, M. L. Metasurfaces for augmented and virtual reality (Conference Presentation). In: *Proc. SPIE 11080, Metamaterials, Metadevices, and Metasystems*. 110800R (San Diego, California, United States: SPIE, 2019).
41. Huang, X. et al. Three-color phase-amplitude holography with a metasurface doublet. In: *Proc Conference on Lasers and Electro-Optics (CLEO)*. 1–2 (San Jose, CA, USA: IEEE, 2020).
42. Shrestha, S., Overvig, A. & Yu, N. Multi-element meta-lens systems for imaging. In: *Proc Conference on Lasers and Electro-Optics (CLEO)*. 1–2 (San Jose, CA, USA: IEEE, 2019).
43. Katsidis, C. C. & Siapkas, D. I. General transfer-matrix method for optical multilayer systems with coherent, partially coherent, and incoherent interference. *Appl. Opt.* **41**, 3978–3987 (2002).
44. Malek, S. C. et al. Active nonlocal metasurfaces. *Nanophotonics* **10**, 655–665 (2020).
45. Meng, Y. et al. Optical meta-waveguides for integrated photonics and beyond. *Light Sci. Appl.* **10**, 235 (2021).
46. Shrestha, S. et al. Broadband achromatic dielectric metalenses. *Light Sci. Appl.* **7**, 85 (2018).